Published in final edited form as:

ACS Chem Biol. 2018 May 18; 13(5): 1322–1332. doi:10.1021/acschembio.8b00116.

Substrate Recognition by a Colistin Resistance Enzyme from *Moraxella catarrhalis*

Peter J. Stogios[†,‡], **Georgina Cox**[§,#], **Haley L. Zubyk**[§], **Elena Evdokimova**[†,‡], **Zdzislaw Wawrzak**[‖], **Gerard D. Wright**[§], and **Alexei Savchenko**[*,†,‡,⊥]

[†]Department of Chemical Engineering and Applied Chemistry, University of Toronto, Toronto, Ontario M5G 1L6, Canada

[‡]Center for Structural Genomics of Infectious Diseases (CSGID)

[§]Department of Biochemistry and Biomedical Sciences, Michael G. DeGroote Institute for Infectious Disease Research, McMaste University, Hamilton, Ontario L8S 4K1, Canada

[‖]LS-CAT, Synchrotron Research Center, Northwestern University, Argonne, Illinois 60439, United States

[⊥]Department of Microbiology, Immunology and Infectious Diseases, Health Research Innovation Centre, University of Calgary, 3330 Hospital Drive NW, HRIC-2C66, Calgary, Alberta T2N 4N1, Canada

Abstract

Lipid A phosphoethanolamine (PEtN) transferases render bacteria resistant to the last resort antibiotic colistin. The recent discoveries of pathogenic bacteria harboring plasmid-borne PEtN transferase (*mcr*) genes have illustrated the serious potential for wide dissemination of these resistance elements. The origin of *mcr-1* is traced to *Moraxella* species co-occupying environmental niches with Enterobacteriaceae. Here, we describe the crystal structure of the catalytic domain of the chromosomally encoded colistin resistance PEtN transferase, ICR^{Mc} (for intrinsic colistin resistance) of *Moraxella catarrhalis*. The ICR^{Mc} structure in complex with PEtN reveals key molecular details including specific residues involved in catalysis and PEtN binding. It also demonstrates that ICR^{Mc} catalytic domain dimerization is required for substrate binding. Our structure-guided phylogenetic analysis provides sequence signatures defining potentially colistin-active representatives in this enzyme family. Combined, these results advance the molecular and mechanistic understanding of PEtN transferases and illuminate their origins.

Graphical Abstract

[*]**Corresponding Author** Alexei Savchenko. alexei.savchenko@ucalgary.ca.
[#]G.C.: Department of Molecular and Cellular Biology, University of Guelph, Guelph, Ontario, Canada N1G 2W1

ASSOCIATED CONTENT

Supporting Information

The Supporting Information is available free of charge on the ACS Publications website at DOI: 10.1021/acschem-bio.8b00116. Sequence alignment of PEtN transferases, size exclusion chromatography of ICR^{Mc}, structure of the active site of the dimeric ICR^{Mc}$_{cat}$^{Thr315Ala}.di-Zn^{2+}.PEG complex, and comparison of the structures of ICR^{Mc} with EptA and EptC (PDF)

Notes

The authors declare no competing financial interest.

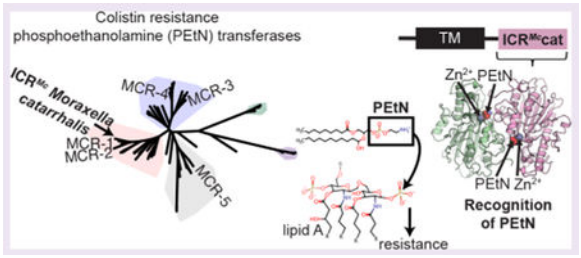

The polymyxin antibiotic colistin is classified as an antibiotic of critical importance by the World Health Organization due to its activity against multidrug resistant Gram-negative pathogens.[1] Colistin is utilized as a treatment of last resort for recalcitrant infections such as those caused by carbapenem-resistant Enterobacteriaceae. Even though colistin is nephrotoxic, the seriousness of such infections and the dearth of alternative treatments has increasingly secured a place for this antibiotic in the infectious disease treatment armory in the absence of new antibiotics.[2]

Many species are intrinsically resistant to polymyxins, including *Neisseria meningitidis*, *Helicobacter pylori*, *Burkholderia cepacia*, and *Moraxella catarrhalis*.[3,4] The mechanisms of resistance harbored by these bacteria include expression of efflux pumps, shedding of capsule polysaccharide, and modification of lipopolysaccharide (LPS), the latter of which appears the most prevalent (reviewed in ref 5). Diverse covalent modifications of LPS, which include among others the addition of phosphoethanolamine (PEtN) groups (reviewed in ref 6) are thought to alter the physical properties of the outer membrane, resulting in polymyxin resistance. The increased clinical and agricultural use of colistin has been linked to the mobilization and transfer of colistin resistance elements to human pathogenic bacteria such as *Escherichia coli*, *Klebsiella pneumoniae*, *Pseudomonas aeruginosa*, and *Acinetobacter baumannii*, representing serious threats to the effectiveness of polymyxins against these species.[3]

Well-characterized representatives of PEtN transferases include EptA from *E. coli*, *Vibrio cholerae*, and *H. pylori*, EptA (originally named LptA) from *N. meningitidis*, PmrC from *A. baumannii*, and CptA from *Campylobacter jejuni* (reviewed in ref 6). These chromosomally encoded enzymes catalyze the transfer of PEtN from phosphatidylethanolamine (PE) onto the lipid A moiety of LPS. *E. coli* EptB is another type of PEtN transferase, which specifically catalyzes the modification of the outer 3-deoxy-D-manno-octulosonic acid (Kdo) residue of LPS.[7]

The recent discovery of the PEtN transferase encoded by the *mcr-1* gene[8] mobilized on a plasmid raised the possibility of accelerated dissemination and acquisition of colistin resistance among pathogens or its collection into multidrug resistance cassettes.[9] Indeed, this gene has since been detected in other Enterobacteriaceae species around the world, in additional patient isolates, and in retrospective searches of culture collections.[10–17] *mcr-1* has also been found on mobile genetic elements containing up to nine other antibiotic resistance genes, including extended-spectrum β-lactamases (ESBLs).[10,14,18] As further evidence of the mobilization of colistin resistance, additional genes encoding PEtN

transferases including *mcr-2*, which shares 81% sequence identity with *mcr-1*, plus the more sequence-distinct *mcr-3*, *mcr-4*, and *mcr-5* have been recently discovered on Enterobacteriaceae plasmids.[19–21] Thus, PEtN transferases have mobilized multiple times and are becoming worrisome resistance determinants that may have serious and long-lasting clinical implications.

Resistance genes manifesting in the clinic can often be traced to environmental and other bacteria, which represent a global reservoir of resistance genes that can be transferred between diverse genera via mobile genetic elements (reviewed in refs 22 and 23). For example, genes conferring clinical levels of antibiotic resistance such as *qnrA* and $bla_{CTX\text{-}M}$ were subsequently traced to aquatic bacteria (reviewed in ref 24). Along the same lines, environmental paralogues were suggested for *mcr-1* and similar PEtN transferase genes. Sequence similarity searches identify close MCR-1 and MCR-2 orthologs (61–65% identity of the full-length protein sequences) in the Moraxellaceae family, specifically in the human pathogen *Moraxella catarrhalis*, the nematode symbiont *Moraxella osloensis*, and the environmental bacteria *Enhydrobacter aerosaccus* and *Psychrobacter* spp.[8] Based on these observations, it was suggested that *Moraxella* species occupying the same ecological niche as *E. coli* encode the ancestral gene of *mcr-1* and *mcr-2*;[19] a subsequent study indeed detected *mcr-1* orthologous genes in numerous *Moraxella* species.[25] Thus, *Moraxella* or related species may represent an ecological reservoir for mobilization of PEtN transferases to other pathogens; however, the molecular and functional characterization of these ancestral MCR-1 proteins has been lacking.

According to sequence analysis, PEtN transferases are comprised of an N-terminal transmembrane region and a periplasm-facing C-terminal hydrolase domain belonging to the alkaline phosphatase superfamily. The periplasmic catalytic domains of MCR-1, MCR-2, EptA, and EptC have been recently structurally characterized. Some of the revealed common molecular features observed in the active site of these enzymes included a conserved catalytic threonine (often covalently linked to phosphate) and multiple Zn^{2+} binding sites.[26–33] The crystal structures of PEtN catalytic domains also featured disulfide bridges between spatially colocalized cysteine residues. These structural data provided the molecular framework for understanding of PEtN transferases; however, the molecular information concerning substrate recognition is still lacking. Furthermore, significant sequence divergence between EptA and EptC and MCR-1 (EptA and EptC both share only 42% sequence identity to MCR-1 in the catalytic domain) necessitates further structural and functional studies into closer representatives of the latter enzyme to define the possible role of these enzymes in development of colistin resistance.

In this study, we characterized the crystal structure of the catalytic domain of the PEtN transferase from *M. catarrhalis* (which we designate as ICR^{Mc}), the protein that represents the closest known ortholog to MCR-1 and MCR-2 and is responsible for intrinsic colistin resistance of this bacterium. Our crystal structures also provide insights into the molecular basis of recognition of the PEtN substrate and identify a putative role of dimerization for resistance activity. Our findings show that MCR-1 and ICR^{Mc} share key structural and functional characteristics in their catalytic domains, supporting the hypothesis that Moraxellaceae are the environmental reservoir of PEtN transferases.

RESULTS AND DISCUSSION

icr^{Mc} Confers Polymyxin Resistance.

To test the ability of ICR^{Mc} to confer resistance, we expressed *icr*^{Mc} in *E. coli* BW25113 and compared its ability to grow in the presence of colistin and polymyxin B with that of the same *E. coli* strain expressing *mcr-1*. Both the *icr*^{Mc} and *mcr-1* expressing strains showed 4–16-fold (depending on promoter strength/expression level[34]) higher resistance to these antibiotics compared to the *E.* coli strain with no expression vector (Table 1). Next we tested whether the expression of the *icr*^{Mc} or *mcr-1* fragments corresponding to the PEtN transferase periplasmic catalytic domain (designed *icr*^{Mc}cat and *mcr-1*cat) in the same *E. coli* strain is sufficient to confer polymyxin resistance. The results showed that *E. coli* harboring *icr*^{Mc}cat or *mcr-1*cat did not show a polymyxin resistance phenotype. These results demonstrated that expression of *icr*^{Mc} confers polymyxin resistance comparable to that of *mcr-1* and that both enzymes require their N-terminal transmembrane regions to confer drug resistance in the cell.

MCR-1, MCR-2, and ICR^{Mc} Define a Distinct Group in the Broader PEtN Transferase Family.

To clarify the phylogenetic relationship between ICR^{Mc} and other PEtN transferases, we performed a phylogenetic reconstruction of the PEtN transferase family, including 89 known MCR and related proteins (Figure 1). This analysis revealed five clades, which segregate along their substrate specificity. One of the clades is represented by MCR-3, MCR-4, and EptA, known to catalyze transfer of PEtN from PE to lipid A. The second one features orthologs of MCR-5 found in *Legionella* species. The third clade is represented by EptB, which acts on Kdo, while the fourth clade includes EptC/CptA, which target lipid A. The fifth clade contains orthologs of MCR-1 and MCR-2, which we termed as MCR-1-like. The five clades show significant divergence reflected in low amino acid sequence similarity between representatives of different clades. Specifically, EptB and MCR-3 shared only 25% and 32% sequence identity with MCR-1. Within the MCR-3/MCR-4/EptA clade, the MCR-3 and MCR-4 enzymes appear to be distinct from the rest of their orthologs, suggesting separate evolutionary paths or ancestral origins. These observations are consistent with multiple incidents of mobilization of intrinsic PEtN ancestral genes leading to diversification among members of this family and reflecting different functional properties.

Consistent with previous reports,[8,25] our phylogenetic reconstruction recapitulated that the MCR-1-like clade contains a closely associated group of sequences from Gammaproteobacteria that share between 57% and 98% sequence identity with MCR-1, including MCR-1, MCR-2, and members in Moraxellaceae species: ICR^{Mc}, ICR$^{M.\ osloensis}$, and ICR$^{E.aerosaccus}$. Beyond this group, the MCR-1-like clade contained a group of uncharacterized proteins, including representatives from *Sulfurospirillum* spp., *Arcobacter* spp., *Campylobacter sputurum* and *Marinobacter subterrani* and these share between 41 and 79% identity with MCR-1. Notably, this group also shares significant similarity with the EptA clade. These observations indicate that the ability to confer colistin resistance established for MCR-1 and ICR^{Mc} may be shared by the wider sequence-related group of PEtN transferases, which forms a distinct clade in the PEtN transferase superfamily.

Alignment of PEtN transferase sequences (Figure S1) revealed higher degree of sequence conservation in the C-terminal region (i.e., 68% sequence identity between ICR^{Mc} and MCR-1 or MCR-2). Combined with the comparable resistance phenotype conferred by expression of these enzymes, this points to strong conservation of functional and structural features between the ICR^{Mc} and MCR-1/MCR-2 enzymes.

Crystal structure of the catalytic domain of ICR^{Mc}.

Next, we purified and crystallized the catalytic domain of ICR^{Mc} (ICR^{Mc}cat) spanning residues 235 to 578 (Figure 2A). The crystal structure of this domain was determined to 2.61 Å by Molecular Replacement using the structure of *N. meningitis* EptA/LptA[26] as a model. The X-ray crystallographic statistics are summarized in Table 2.

The crystal structure contains one copy of the ICR^{Mc}cat domain in the asymmetric unit. Residues 244 through 578 could be traced in the electron density, while residues 235–243 appear disordered. The resolved ICR^{Mc}cat residues adopted the common sulfatase/hydrolase fold, characterized by a central seven-stranded β-sheet mainly parallel in topology, with the edge strand β12 oriented in an antiparallel orientation (Figure 2A).

The structure of ICR^{Mc}cat reveals two unambiguous disulfide bonds (Cys390 to Cys398, Cys448 to Cys456). Another pair of cysteine residues, Cys311 and Cys321 appear reduced; however the proximity of their side chains suggests the possibility of formation of an additional disulfide bond (Figure 2A). We interpreted additional difference electron density in the structure as six sulfate ions and one phosphate ion. Unexpectedly, the ICR^{Mc}cat crystal structure did not contain additional electron density corresponding to the Zn^{2+} ion required for PEtN transferases.[26,27,29–33] Interpreting this as possible depletion of Zn^{2+} ions in the course of ICR^{Mc}cat purification, we soaked ICR^{Mc}cat protein crystals in zinc chloride-supplemented buffer (see Methods for details). We detected significant anomalous diffraction at the Zn^{2+} dispersion absorption peak for such crystals and identified additional electron density corresponding to a single Zn^{2+} atom bound to ICR^{Mc}cat active site (Figure 2A, Figure 3).

The active site region of ICR^{Mc}cat localized to a small (~200 Å^3) pocket at the “top” of the central β-sheet (as shown in Figure 2B) lined by residues from converging loops. This pocket was on the large, flat face of the ICR^{Mc}cat domain close to its N-terminus. Apart from the Zn^{2+}, the active site contains a phosphate ion at 3.7 Å distance from the Zn^{2+}, which is anchored by a network of interactions with the active site residues (Figure 3). The Zn^{2+} ion is coordinated primarily by the side chains of Glu273, Thr315, Asp498, and His499. The phosphate forms interactions with the side chain hydroxyl and backbone amide of Thr315, the side chain of His511, and two ordered water molecules, one of which also interacted with the Zn^{2+} ion. The Zn^{2+} and phosphate-binding residues are in turn oriented by a network of interactions with other active site residues including Asn359, Ser360, and His424. Notably, Thr315 in the ICR^{Mc}cat active site occupies the position corresponding to the phosphate-accepting nucleophilic residue in the other PEtN transferases.[26,27,29–32] Analysis of ICR^{Mc}cat residues interacting with both Zn^{2+} and the phosphate ions also highlights His429 as a functionally important residue, although its interaction with the Zn^{2+} was mediated through a hydrogen bond with the coordinated water molecule. In addition to

the Zn^{2+} and phosphate ions, the ICR^{Mc}cat active site contained a sulfate ion positioned at 11 Å distance from the phosphate ion described above. The sulfate forms close interactions with Arg436, which in turn forms a salt bridge with Glu397. In total, our analysis suggested that at least 18 ICR^{Mc} active site residues participate in interactions with the Zn^{2+}, phosphate, and sulfate ligands.

Substrate Recognition Requires the Dimerization of the ICR^{Mc}cat Domain.

To characterize the molecular basis of substrate recognition by ICR^{Mc}cat, we crystallized the Thr315Ala ICR^{Mc}cat variant in the presence of the disaccharide headgroup of lipid A or PEtN, a component of the lipid substrate phosphatidylethanolamine. Thr315 is predicted to be the nucleophilic residue that attacks the substrate phosphate group. Consistent with this prediction, mutation to Ala abolishes antibiotic resistance activity (Table 1). This crystal structure was determined to 1.64 Å (Table 2) and revealed a different unit cell and packing compared to the wild-type ICR^{Mc}cat. In contrast to the ICR^{Mc}cat apo structure, the ICR^{Mc}cat^{Thr315Ala}.mono-Zn^{2+}.PEtN complex structure features two ICR^{Mc}cat^{Thr315Ala} molecules associated as a homodimer with ~1190 $\sim^2$ buried at the dimerization interface. The ICR^{Mc}cat protein chains in the PEtN complex structure associate in a symmetrical “front-to-front” orientation, with the two active sites facing each other (Figure 4A,B). Dimerization involves interactions between 38 residues in each monomer and impacts both the shape and accessibility of the active sites. In the ICR^{Mc}cat dimer, the entrance to the catalytic centers is buried along the dimerization interface with access through deep clefts formed by this interface (Figure 4C). Consistent with this observed association of ICR^{Mc}cat domains, we also detected the formation of a dimer in solution by size exclusion chromatography, which is more prominent in the presence of Zn^{2+} ions (Figure S2).

Well-defined additional electron density allowed unambiguous positioning of one PEtN molecule in each active site of the ICR^{Mc}cat^{Thr315Ala} dimer in the complex structure (Figure 5). The phosphate of the PEtN molecule forms interactions with the Zn^{2+} ion and the side chain of His511, as well with the backbone of Ala315 and three water molecules. Intriguingly, the Tyr338 from the partner monomer chain also contributes to coordination of the substrate molecule (Figure 5). Notably, the position of the phosphate group of the PEtN molecule in the complex structure corresponds to the position of the phosphate ion in the apo structure. Orientation of the PEtN molecule in the ICR^{Mc}cat active site is consistent with the predicted catalytic mechanism of this family whereby a threonine residue (Thr315 in ICR^{Mc}) performs nucleophilic attack on the phosphate atom of the phosphatidylethanolamine substrate to generate a phosphoethanolamine–Thr intermediate species. We did not observe any interactions between the ethanolamine moiety of PEtN and the enzyme. Taken together, the structural analysis of the ICR^{Mc}cat^{Thr315Ala}. PEtN complex suggests that dimerization of this domain may facilitate the coordination of the substrate providing an additional interaction partner (Tyr338) from the adjacent subunit that may be required for optimal positioning of the phosphatidylethanolamine substrate for catalysis.

One of the tested ICR^{Mc}cat^{Thr315Ala} crystals obtained in the presence of lipid A headgroup lacked additional density corresponding to the substrate molecule but featured a second Zn^{2+} ion (Zn2 in Figure S3) in the active sites of the ICR^{Mc}cat dimer. The position of Zn2

corresponds to that of the phosphate of PEtN in the complex structure. In this structure, the Zn2 is coordinated by side chains of residues Glu273, His429, and His511 and the backbone amide of Ala315. In this interaction, the His429 underwent a rotamer change relative to its position in the ICR^{Mc} apo structure. Thus, there could be an interplay between the binding of a second Zn^{2+} atom and the phosphate groups of the enzyme's substrates. Furthermore, the active sites of the ICR^{Mc}cat^{Thr315Ala}.di-Zn^{2+} structure contain elongated difference electron density corresponding to a poly(ethylene glycol) molecule present in the crystallization solution (Figure S3). The position of this molecule in the active site approaches the catalytic center of the enzyme and forms a packing interaction against His429 and hydrophobic interactions with Met426 and the aliphatic region of the Lys378 side chain. Accordingly, we propose that the position of the poly(ethylene glycol) molecule may be indicative of the position of the lipid A headgroup in the ICR^{Mc}cat active site.

Guided by our structural analysis, we tested the roles of ICR^{Mc}cat residues implicated in interactions with Zn^{2+} and PEtN by site-directed mutagenesis. Residues Thr315, His429, Arg436, and Tyr338 were individually mutated to Ala in the context of the full-length ICR^{Mc} protein. The *E. coli* strains expressing the corresponding ICR^{Mc} variants completely lost resistance to colistin and polymyxin B compared to the strain carrying the wild-type enzyme, confirming the important role of these residues for ICR^{Mc} activity (Table 1). Based on these results, we postulate that coordination of Zn^{2+} binding by Thr315, His429, and Tyr338 residues and unexpectedly, interactions of residues Tyr338 and Arg436 with substrate molecules as facilitated by ICR^{Mc}cat domain dimerization, may be essential for the catalytic activity of ICR^{Mc}.

Comparative Structural Analysis Highlights Signature Active Site Features of the PEtN Transferase Family.

We conducted a comparative analysis of this structure versus those of recently characterized MCR-1 and MCR-2 resistance enzymes as well as the structures of previously characterized EptA and EptC to clarify the shared and distinct features of these PEtN transferases.

The ICR^{Mc} structure superimposes with that of MCR-1 and MCR-2 with RMSD of 0.5 and 0.5 Å over 251 and 270 matching Cα atoms, respectively (Figure 6). This superimposition reveals only minor structural differences primarily in conformations of the $\beta5$–$\eta4$ and $\beta6$–$\eta5$ loops. More importantly, all 18 residues of the active site (Figure 6) are absolutely conserved across these three enzymes. Furthermore, these 18 amino acids, which include the histidine (His429) residue undergoing rotation between binding to PEtN or Zn^{2+} ion in ICR^{Mc} structures, are universally conserved across the MCR-1-like PEtN transferases (Figure S1). Interestingly, the Tyr338 residue, whose role in PEtN binding is facilitated by catalytic domain dimerization, is also conserved in the orthologs of ICR^{Mc}, MCR-1 and MCR-2. This observation prompted us to suggest that the active site architecture, binding mode of PEtN, and coordination of substrates across a dimer interface as visualized in the ICR^{Mc} cat–PEtN complex structure is conserved across the MCR-1-like clade of PEtN transferases defined above.

Expanding our structure-based sequence analysis to the recently identified MCR-3, MCR-4 and MCR-5 enzymes revealed conservation of 12 out of 18 active site residues invariable in

MCR-1-like enzymes (Figure S1). These include residues involved in coordination of the Zn^{2+} ion and in catalysis. Notably, we were not able to identify the equivalent of ICR^{Mc}cat residue Tyr338 in MCR-3 or MCR-4. These differences may be indicative of deviation in substrate-binding mode between MCR-1-like PEtN transferases and the MCR-3, MCR-4, and MCR-5 enzymes.

Detailed comparative analysis of ICR^{Mc} and EptA and EptC revealed differences in the conformations of the $\beta5$–$\eta4$ and $\beta6$–$\eta5$ loops and in active site composition (Figure S4). Of the 18 active site residues in MCR-1-like enzymes described above, only 11 are conserved in EptA and EptC (Figures S1 and S4). Once again, the conserved residues in EptA and EptC active sites cluster to the Zn^{2+} binding sites, consistent with a common catalytic mechanism shared across the entire PEtN transferase family. In contrast, the four nonconserved residues corresponding to ICR^{Mc} residues Asn359, Ser360, Lys378, and Met426 cluster together and away from the Zn^{2+} binding site. Identification of these subtle differences may be reflective of EptA and EptC deviating in substrate preference from MCR-1-like enzymes.

Our observation that the dimeric state of ICR^{Mc}cat^{Thr315Ala} forms a solvent-occluded pocket containing a PEG molecule suggests that only in the dimer state of the catalytic domain or in the context of the full-length protein containing the transmembrane region is the protein capable of forming an active site structure that can recognize the larger lipid A substrate. Indeed, analysis of the crystal structure of EptA, the MCR-1 ortholog from *N. meningitidis*, suggested that the membrane-spanning portion and the linker to the catalytic domain are involved in mediating substrate interactions.[35] The detergent (DDM) molecule trapped in the membrane-spanning portion of EptA is oriented toward the active site of the catalytic domain suggesting it mimics the position of enzyme's substrate (Figure 7). With our ICR^{Mc}cat^{Thr315Ala}.PEtN crystal structure in hand, we are able to posit a model of the ternary complex with a lipid positioned to attack the phosphoethanolamine–threonine intermediate (Figure 7). This model was developed through a superposition of the structures of EptA. DDM and ICR^{Mc}cat^{Thr315Ala}.PEtN, which showed that the position of these two ligands do not overlap: more specifically, the O3B of DDM and O3 of PEtN approached each other in this model, and thus this overlay can be used to interpret the position of a phosphorylated lipid molecule in the active site (Figure 7). This model also validates the prediction that EptA Glu114 interacts with the amine group of PEtN[35] as this residue and its equivalent in ICR^{Mc} (E113) is positioned within bonding distance to this functional group. Consistent with its functional importance, this glutamate residue is conserved throughout the PEtN transferase family (except for the EptB subgroup), suggesting it plays a role in discrimination for PE. Further structural and enzymatic studies into PEtN transferase and their interactions with native substrates are required to further validate this model and reveal additional key details.

The binding of substrates may require ICR^{Mc}cat domain dimerization, which according to our structural analysis provides additional interaction partners for the substrate molecules in both actives sites of the dimer. A molecular dynamics simulation of EptA[35] showed that the soluble domain can adopt multiple conformations and "roll" over the simulated membrane surface, indicating that the dimerization interface we observed in ICR^{Mc} complex structure may be accommodated in such a fluid situation.

Our demonstration of the conservation of the molecular details of the ICR^{Mc}, MCR-1, and MCR-2 active sites supports the notion that *Moraxella* species form the reservoir of at least this group of PEtN transferases. This stresses that structural and functional studies of intrinsic resistance enzymes in species cohabitating environmental niches as human pathogens are key components of developing a better understanding of the origins and mechanisms of resistance impacting clinical management of pathogens. As has been evidenced in numerous examples, and even in the ongoing discovery of new *mcr* genes, the source of clinical antibiotic resistance is the environment. Progress toward developing a complete understanding of the broader resistome, such as our characterization of ICR^{Mc}, is a key component of resistance surveillance and anticipation of future mobilization events.

Finally, our structure-based phylogenetic analysis provides a foundational organization of PEtN transferases that clearly shows that these enzymes are diverse in sequence and each discovery of novel *mcr* genes identifies founding members of subclasses of PEtN transferases. This phenomenon parallels the expansion of β-lactamase families over the course of decades of β-lactam clinical deployment[36] and underscores the extent of the dissemination of polymyxin resistance. As with β-lactamase family-specific properties, functional insights into individual PEtN transferases may not be conserved across the subgroups. Thus, appreciation of the structural and molecular diversity of MCR enzymes is critical for drug discovery efforts against these enzymes.

METHODS

MIC Determination.

Full-length *icr*^{Mc} and its catalytic domain (*icr*^{Mc}cat; residues 235–578) plus full-length *E. coli mcr-1* and its catalytic domain (*mcr-1*cat; residues 208–541) were ligated into the pGDP1 and pGDP2 vectors (in house derivatives of the pBR322 vector; New England BioLabs). These plasmids utilize constitutive promoters of differing strength; the stronger β-lactamase P_{bla} promoter (pGDP1) and the weaker P_{lac} promoter (pGDP2). Amino acid substitutions in *icr*^{Mc} were performed using Phusion High-Fidelity DNA Polymerase (Thermo Scientific) and the pGDP1:*icr*^{Mc} construct. Constructs were confirmed by sequencing (Central MOBIX facility, McMaster University). Susceptibility testing (in triplicate, with two biological replicates) was performed with *E. coli* BW25113 cultured in Mueller-Hinton II broth (cation adjusted) (Becton, Dickinson and Co, Franklin Lakes NJ) using the broth microdilution method according to CLSI guidelines. Inoculum was prepared using the colony resuspension method, and plates were incubated with aeration at 37 °C for 18 h.

Protein Expression and Purification.

cDNA of *icr*^{Mc} from *Moraxella catarrhalis* strain BC1 (Genbank accession EGE18576) coding for residues 235 to 578 of ICR^{Mc} was synthesized by Integrated DNA Technologies and subcloned into the pMCSG53 expression vector, which codes for an N-terminal His_6-tag and a TEV protease cleavage site. *icr*^{Mc} was expressed in *E. coli* BL21(DE3) Gold cells, grown to an OD_{600} of 0.6 at 37 °C, chilled to 16 °C, and induced overnight with 500 μM isopropyl β-D-thiogalactopyranoside. Cells were harvested via centrifugation at 5000 × *g*,

pellets were resuspended in binding buffer [50 mM Hepes (pH 7.5), 100–300 mM sodium chloride, 10 mM imidazole, and 2% glycerol (v/v)] and lysed by sonication, and cell debris was removed via centrifugation at 30000 × *g*. Cleared lysate was loaded onto a 5 mL Ni-NTA column (QIAGEN) pre-equilibrated with binding buffer and extensively washed with binding buffer containing 30 mM imidazole, and protein was eluted using the above buffer with 250 mM imidazole. Fractions containing ICR^{Mc} were identified by SDS–polyacrylamide gel electrophoresis and further purified via gel filtration on a HiLoad 16/60 Superdex75 prep-grade column [10 mM Hepes (pH 7.5) and 50 mM potassium chloride].

Crystallization and Structure Determination.

All crystallization was performed at RT using the sitting drop method and 2 μL of protein or protein/ligand mixture plus 2 μL of reservoir solution. Zn^{2+}-free ICR^{Mc} was crystallized with reservoir solution 0.1 M sodium acetate, pH 4.6, and 1.2 M ammonium sulfate, and the crystal was cryoprotected in 8% glycerol, 8% ethylene glycol, and 8% sucrose. Crystals of Zn^{2+}-bound mono-Zn^{2+}.ICR^{Mc} were obtained by soaking apo crystals with 2.5 mM zinc chloride for 30 min followed by cryoprotection in the above cryosolution. Crystals of ICR^{Mc}cat^{Thr315Ala}. mono-Zn^{2+}.PEtN were obtained from reservoir solution 0.1 M MES, pH 6, 22% (w/v) PEG 400, 2.5 mM zinc chloride, and 5 mM PEtN, and the crystal was cryoprotected in paratone oil. Crystals of ICR^{Mc}cat^{Thr315Ala}.di-Zn^{2+}.PEG were obtained from reservoir solution 0.1 M Tris, pH 8, 28% (w/v) PEG 4000, 3 mM zinc chloride, and 2 mM lipid A headgroup (Glycobiotech GmbH), and the crystal was cryoprotected in paratone oil. All X-ray diffraction data at 100 K were collected at the Advanced Photon Source, Argonne National Laboratory, Life Sciences Collaborative Access Team beamline 21-ID-D at the following wavelengths corresponding to the measured zinc absorption peak: ICR^{Mc}.PO_4, 1.27424 Å/9730 keV; ICR^{Mc}.mono-Zn^{2+}, 1.27424 Å/9730 keV; ICR^{Mc}cat^{Thr315Ala}.mono-Zn^{2+}.PEtN, 1.27687 Å/9710 keV; ICR^{Mc}cat^{Thr315Ala}.di-Zn^{2+}.PEG, 1.27815 A/9700 keV. X-ray data were reduced with XDS[37] and CCP4 Aimless[38] or HKL-3000[39] for the di-Zn^{2+}.PEG structure. The WT structures were solved by molecular replacement using the ICR^{Mc} sequence-substituted structure of *Neisseria meningitis* EptA/LptA (PDB id 4kay[26]) using Phenix.-phaser,[40] while the ICR^{Mc}cat^{Thr315Ala} structures were phased using the anomalous signal from Zn^2. Refinement was completed with Phenix.refine and Coot.[41] All B-factors were refined as isotropic with TLS parametrization. Zn^{2+}, sulfate ions, and the positions of the six cysteine residues implicated in disulfide bond formation were verified by the presence of peaks in omit or anomalous difference maps. In the WT ICR^{Mc} structure, the peak in the anomalous difference electron density peak was 32σ, 0.148 e^-/A^3. With respect to Zn^{2+} atoms, in the ICR^{Mc}cat^{Thr315Ala}.di-Zn^{2+} structure, the anomalous difference density peak heights were 91σ, 0.896 e^-/A^3, and 82σ, 0.827 e^-/A^3, in one active site and 85σ, 0.839 e^-/A^3, and 84σ, 0.828 e^-/A^3, in the second active site. In the ICR^{Mc}cat^{Thr315Ala}.mono-Zn^{2+}.PEtN complex, the anomalous different density peak heights were 95.0σ, 0.96 e^-/A^3, and 81.6σ, 0.86 e^-/A^3, in one active site and 85.3σ, 0.90 e^-/A^3, and 84.3σ, 0.89 e^-/A^3, in the second active site. All geometry was verified using the Phenix and the wwPDB server.

Sequence and Structural Analysis.

Sequence orthologs of ICR^{Mc}, MCR-1, MCR-2, MCR-3, MCR-4, EptA, EptB, and EptC, were identified in Genbank using BLAST. Sequence alignment was performed using Jalview[42] and verified by eye and inspection of structural features of ICR^{Mc}. Sequence alignment was produced by ESPript.[43] Phylogenetic reconstruction was conducted using the aligned full-length PEtN transferase sequences and the program Mr. Bayes.[44] Structure similarity searches were performed using the Dali server.[45] Active site volume was calculated by the CastP server.[46] Model of full-length ICR^{Mc} onto EptA was constructing using Phyre2.[47] Dimerization interface burial in the ICR^{Mc}cat^{Thr315Ala} crystal structure was calculated using the PDBePISA server[48] and experimentally tested in solution using a Superdex S200 size exclusion column.

Supplementary Material

Refer to Web version on PubMed Central for supplementary material.

ACKNOWLEDGMENTS

We thank R. Di Leo for cloning. The structures presented were solved by the Center for Structural Genomics of Infectious Diseases (CSGID, http://csgid.org); this project has been funded in whole or in part with U.S. Federal funds from the National Institute of Allergy and Infectious Diseases, National Institutes of Health, Department of Health and Human Services, under Contract Numbers HHSN272201200026C and HHSN272201700060C. This research was supported by the Ontario Research Fund Research Excellence (ORF-RE) Grant No. RE07-048 (to G. D. Wright and A. Savchenko). This research was also supported by a Canadian Institutes of Health Research grant (FRN-148463) and by a Canada Research Chair in Antibiotic Biochemistry (to G. D. Wright).

REFERENCES

(1). World Health Organization (WHO). (2013) Integrated surveillance of antimicrobial resistance: guidance from a WHO Advisory Group.

(2). Rafailidis PI, and Falagas ME (2014) Options for treating carbapenem-resistant Enterobacteriaceae. Curr. Opin. Infect. Dis 27, 479–483. [PubMed: 25259809]

(3). Olaitan AO, Morand S, and Rolain J-M (2014) Mechanisms of polymyxin resistance: acquired and intrinsic resistance in bacteria. Front. Microbiol 5, 643. [PubMed: 25505462]

(4). Storm DR, Rosenthal KS, and Swanson PE (1977) Polymyxin and related peptide antibiotics. Annu. Rev. Biochem 46, 723–763. [PubMed: 197881]

(5). Baron S, Hadjadj L, Rolain J-M, and Olaitan AO (2016) Molecular mechanisms of polymyxin resistance: knowns and unknowns. Int. J. Antimicrob. Agents 48, 583. [PubMed: 27524102]

(6). Needham BD, and Trent MS (2013) Fortifying the barrier: the impact of lipid A remodelling on bacterial pathogenesis. Nat. Rev. Microbiol 11, 467–481. [PubMed: 23748343]

(7). Reynolds CM, Kalb SR, Cotter RJ, and Raetz CRH (2005) A phosphoethanolamine transferase specific for the outer 3-deoxy-D-manno-octulosonic acid residue of *Escherichia coli* lipopolysaccharide. Identification of the eptB gene and Ca^{2+} hypersensitivity of an eptB deletion mutant. J. Biol. Chem 280, 21202–21211. [PubMed: 15795227]

(8). Liu Y-Y, Wang Y, Walsh TR, Yi L-X, Zhang R, Spencer J, Doi Y, Tian G, Dong B, Huang X, Yu L-F, Gu D, Ren H, Chen X, Lv L, He D, Zhou H, Liang Z, Liu J-H, and Shen J (2016) Emergence of plasmid-mediated colistin resistance mechanism MCR-1 in animals and human beings in China: a microbiological and molecular biological study. Lancet Infect. Dis 16, 161–168. [PubMed: 26603172]

(9). Nordmann P, and Poirel L (2016) Plasmid-mediated colistin resistance: an additional antibiotic resistance menace. Clin. Microbiol. Infect 22, 398. [PubMed: 27021419]

(10). McGann P, Snesrud E, Maybank R, Corey B, Ong AC, Clifford R, Hinkle M, Whitman T, Lesho E, and Schaecher KE (2016) *Escherichia coli* Harboring *mcr-1* and bla_{CTX-M} on a Novel IncF Plasmid: First Report of *mcr-1* in the United States. Antimicrob. Agents Chemother 60, 4420–4421. [PubMed: 27230792]

(11). Malhotra-Kumar S, Xavier BB, Das AJ, Lammens C, Hoang HTT, Pham NT, and Goossens H (2016) Colistin-resistant *Escherichia coli* harbouring *mcr-1* isolated from food animals in Hanoi, Vietnam., Lancet Infect. Dis 16, 286–287. [PubMed: 26774248]

(12). Poirel L, Kieffer N, Liassine N, Thanh D, and Nordmann P (2016) Plasmid-mediated carbapenem and colistin resistance in a clinical isolate of *Escherichia coli*. Lancet Infect. Dis 16, 281.

(13). Skov RL, and Monnet DL (2016) Plasmid-mediated colistin resistance *(mcr-1* gene): three months later, the story unfolds. Euro Surveill. 21, 30155. [PubMed: 26967914]

(14). Zurfluh K, Klumpp J, Nüesch-Inderbinen M, and Stephan R (2016) Full-length nucleotide sequences of *mcr-1*-harboring plasmids isolated from extended-spectrum-β-lactamase-producing *Escherichia coli* isolates of different origins. Antimicrob. Agents Chemother 60, 5589–5591. [PubMed: 27324774]

(15). Li A, Yang Y, Miao M, Chavda KD, Mediavilla JR, Xie X, Feng P, Tang Y-W, Kreiswirth BN, Chen L, and Du H (2016) Complete Sequences of *mcr-1*-Harboring Plasmids from Extended-Spectrum-β-Lactamase- and Carbapenemase-Producing. Antimicrob. Agents Chemother 60, 4351–4354. [PubMed: 27090180]

(16). Yao X, Doi Y, Zeng L, Lv L, and Liu J-H (2016) Carbapenem-resistant and colistin-resistant *Escherichia coli* co-producing NDM-9 and MCR-1. Lancet Infect. Dis 16, 288–289. [PubMed: 26842777]

(17). Haenni M, Poirel L, Kieffer N, Châtre P, Saras E, Métayer V, Dumoulin R, Nordmann P, and Madec J-Y (2016) Cooccurrence of extended spectrum β lactamase and MCR-1 encoding genes on plasmids. Lancet Infect. Dis 16, 281–282.

(18). Malhotra-Kumar S, Xavier BB, Das AJ, Lammens C, Butaye P, and Goossens H (2016) Colistin resistance gene *mcr-1* harboured on a multidrug resistant plasmid. Lancet Infect. Dis 16, 283–284. [PubMed: 26774247]

(19). Xavier BB, Lammens C, Ruhal R, Kumar-Singh S, Butaye P, Goossens H, and Malhotra-Kumar S (2016) Identification of a novel plasmid-mediated colistin-resistance gene, *mcr-2* in *Escherichia coli*, Belgium, June 2016. Euro Surveill. 21, 30280.

(20). Yin W, Li H, Shen Y, Liu Z, Wang S, Shen Z, Zhang R, Walsh TR, Shen J, and Wang Y (2017) Novel Plasmid-Mediated Colistin Resistance Gene *mcr-3* in *Escherichia coli*. mBio 8, e00543–17. [PubMed: 28655818]

(21). Borowiak M, Fischer J, Hammerl JA, Hendriksen RS, Szabo I, and Malorny B (2017) Identification of a novel transposon-associated phosphoethanolamine transferase gene, *mcr-5*, conferring colistin resistance in d-tartrate fermenting *Salmonella enterica* subsp. *enterica* serovar Paratyphi B. J. Antimicrob. Chemother 72, 3317–3324. [PubMed: 28962028]

(22). Surette MD, and Wright GD (2017) Lessons from the Environmental Antibiotic Resistome. Annu. Rev. Microbiol 71, 309–329. [PubMed: 28657887]

(23). Crofts TS, Gasparrini AJ, and Dantas G (2017) Next-generation approaches to understand and combat the antibiotic resistome. Nat. Rev. Microbiol 15, 422–434. [PubMed: 28392565]

(24). Perry JA, and Wright GD (2014) Forces shaping the antibiotic resistome. BioEssays 36, 1179–1184. [PubMed: 25213620]

(25). Kieffer N, Nordmann P, and Poirel L (2017) Moraxella Species as Potential Sources of MCR-Like Polymyxin Resistance Determinants. Antimicrob. Agents Chemother 61, e00129–17. [PubMed: 28320720]

(26). Wanty C, Anandan A, Piek S, Walshe J, Ganguly J, Carlson RW, Stubbs KA, Kahler CM, and Vrielink A (2013) The structure of the neisserial lipooligosaccharide phosphoethanolamine transferase A (LptA) required for resistance to polymyxin. J. Mol. Biol 425, 3389–3402. [PubMed: 23810904]

(27). Fage CD, Brown DB, Boll JM, Keatinge-Clay AT, and Trent MS (2014) Crystallographic study of the phosphoethanolamine transferase EptC required for polymyxin resistance and motility in

Campylobacter jejuni. Acta Crystallogr., Sect. D: Biol. Crystallogr 70, 2730–2739. [PubMed: 25286856]

(28). Cullen TW, Madsen JA, Ivanov PL, Brodbelt JS, and Trent MS (2012) Characterization of unique modification of flagellar rod protein FlgG by *Campylobacter jejuni* lipid A phosphoethanolamine transferase, linking bacterial locomotion and antimicrobial peptide resistance. J. Biol. Chem 287, 3326–3336. [PubMed: 22158617]

(29). Hu M, Guo J, Cheng Q, Yang Z, Chan EWC, Chen S, and Hao Q (2016) Crystal Structure of *Escherichia coli* originated MCR-1, a phosphoethanolamine transferase for Colistin Resistance. Sci. Rep 6, 38793. [PubMed: 27958270]

(30). Hinchliffe P, Yang QE, Portal E, Young T, Li H, Tooke CL, Carvalho MJ, Paterson NG, Brem J, Niumsup PR, Tansawai U, Lei L, Li M, Shen Z, Wang Y, Schofield CJ, Mulholland AJ, Shen J, Fey N, Walsh TR, and Spencer J (2017) Insights into the Mechanistic Basis of Plasmid-Mediated Colistin Resistance from Crystal Structures of the Catalytic Domain of MCR-1. Sci Rep 7, 39392. [PubMed: 28059088]

(31). Ma G, Zhu Y, Yu Z, Ahmad A, and Zhang H (2016) High resolution crystal structure of the catalytic domain of MCR-1. Sci. Rep 6, 39540. [PubMed: 28000749]

(32). Stojanoski V, Sankaran B, Prasad BVV, Poirel L, Nordmann P, and Palzkill T (2016) Structure of the catalytic domain of the colistin resistance enzyme MCR-1. BMC Biol. 14, 81. [PubMed: 27655155]

(33). Coates K, Walsh TR, Spencer J, and Hinchliffe P (2017) 1.12 Å resolution crystal structure of the catalytic domain of the plasmid-mediated colistin resistance determinant MCR-2. Acta Crystallogr., Sect. F: Struct. Biol. Commun 73, 443–449. [PubMed: 28777086]

(34). Cox G, Sieron A, King AM, De Pascale G, Pawlowski AC, Koteva K, and Wright GD (2017) A Common Platform for Antibiotic Dereplication and Adjuvant Discovery. Cell Chem. Biol 24, 98–109. [PubMed: 28017602]

(35). Anandan A, John CM, Jarvis GA, Vrielink A, O'Mara ML, et al. (2017) Structure of a lipid A phosphoethanolamine transferase suggests how conformational changes govern substrate binding. Proc. Natl. Acad. Sci. U. S. A 114, 2218–2223. [PubMed: 28193899]

(36). Bush K (2013) Proliferation and significance of clinically relevant β-lactamases. Ann. N. Y. Acad. Sci 1277, 84–90. [PubMed: 23346859]

(37). Kabsch W (2010) XDS. Acta Crystallogr., Sect. D: Biol. Crystallogr 66, 125–132. [PubMed: 20124692]

(38). Winn MD, Ballard CC, Cowtan KD, Dodson EJ, Emsley P, Evans PR, Keegan RM, Krissinel EB, Leslie AGW, McCoy A, McNicholas SJ, Murshudov GN, Pannu NS, Potterton EA, Powell HR, Read RJ, Vagin A, and Wilson KS (2011) Overview of the CCP4 suite and current developments. Acta Crystallogr., Sect. D: Biol. Crystallogr 67, 235–242. [PubMed: 21460441]

(39). Minor W, Cymborowski M, Otwinowski Z, and Chruszcz M (2006) HKL-3000: the integration of data reduction and structure solution-from diffraction images to an initial model in minutes. Acta Crystallogr., Sect. D: Biol. Crystallogr 62, 859–866. [PubMed: 16855301]

(40). Adams PD, Afonine PV, Bunkóczi G, Chen VB, Davis IW, Echols N, Headd JJ, Hung LW, Kapral GJ, Grosse-Kunstleve RW, McCoy AJ, Moriarty NW, Oeffner R, Read RJ, Richardson DC, Richardson JS, Terwilliger TC, and Zwart PH (2010) PHENIX: a comprehensive Python-based system for macromolecular structure solution. Acta Crystallogr., Sect. D: Biol. Crystallogr 66, 213–221. [PubMed: 20124702]

(41). Emsley P, and Cowtan K (2004) Coot: model-building tools for molecular graphics. Acta Crystallogr., Sect. D: Biol. Crystallogr 60, 2126–2132. [PubMed: 15572765]

(42). Waterhouse AM, Procter JB, Martin DMA, Clamp M, and Barton GJ (2009) Jalview Version 2-a multiple sequence alignment editor and analysis workbench. Bioinformatics 25, 1189–1191. [PubMed: 19151095]

(43). Robert X, and Gouet P (2014) Deciphering key features in protein structures with the new ENDscript server. Nucleic Acids Res. 42, W320–4. [PubMed: 24753421]

(44). Ronquist F, and Huelsenbeck JP (2003) MrBayes 3: Bayesian phylogenetic inference under mixed models. Bioinformatics 19, 1572–1574. [PubMed: 12912839]

(45). Holm L, and Rosenström P (2010) Dali server: conservation mapping in 3D. Nucleic Acids Res 38, W545–9. [PubMed: 20457744]

(46). Dundas J, Ouyang Z, Tseng J, Binkowski A, Turpaz Y, and Liang J (2006) CASTp: computed atlas of surface topography of proteins with structural and topographical mapping of functionally annotated residues. Nucleic Acids Res. 34, W116–8. [PubMed: 16844972]

(47). Kelley LA, Mezulis S, Yates CM, Wass MN, and Sternberg MJE (2015) The Phyre2 web portal for protein modeling, prediction and analysis. Nat. Protoc 10, 845–858. [PubMed: 25950237]

(48). Krissinel E, and Henrick K (2007) Inference of macromolecular assemblies from crystalline state. J. Mol. Biol 372, 774–797. [PubMed: 17681537]

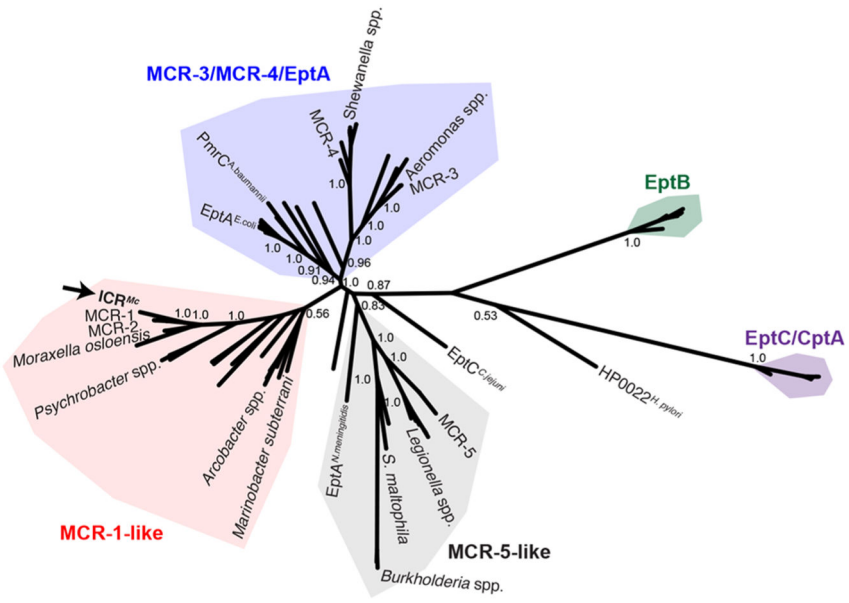

Figure 1.

Phylogenetic relationships of PEtN transferases. The four major clades are independently colored and labeled. Nodes are labeled by Bayesian probability. Arrow labels ICR^{Mc} sequence. Protein sequences with an assigned name are labeled with the name plus originating species in superscript initials; those proteins identified in mobile elements are labeled with the protein name only. Protein sequences without an assigned name are indicated only with the species name.

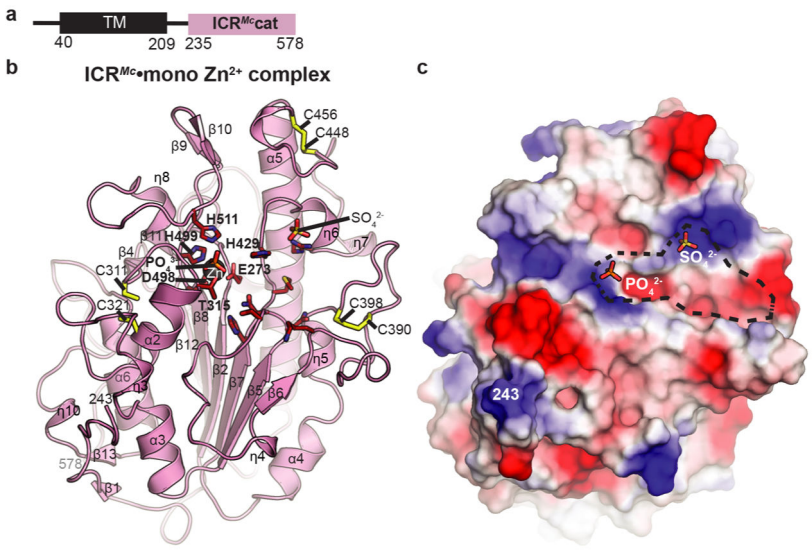

Figure 2.

Structure of ICR^{Mc}.mono-Zn^{2+} complex. (A) Domain architecture, with termini of the TM and catalytic domains indicated. (B) Overall structure. Secondary structure elements are labeled; active site sulfate, phosphate molecules, and amino acids are shown in sticks, Zn^{2+} ion is shown as a black sphere, and cysteine and disulfide bonds are shown with yellow sticks. (C) Electrostatic surface representation. Scale of colors is from red = −10 k_B/T, white = 0, blue = +10. The N-terminus of this domain (residue 243) is labeled. Sticks are shown for active site phosphate and sulfate molecules. Dashed black line indicates active site cleft.

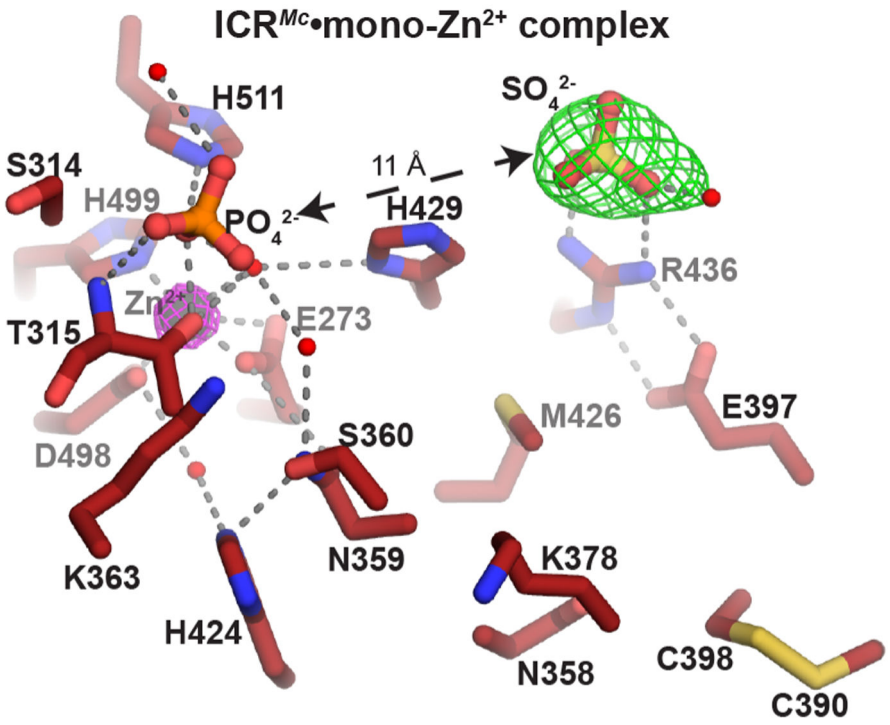

Figure 3.

Active site of ICR^{Mc}.mono-Zn^{2+} complex. The Zn^{2+} ion is shown as a gray sphere with purple electron density (anomalous difference map contoured at 20σ), sulfate electron density is $F_o - F_c$ difference map contoured at 5σ. Dashes indicate hydrogen bonds or salt bridge interactions. Water molecules are shown as red spheres. The distance between the Zn^{2+} ion and sulfate ion is indicated.

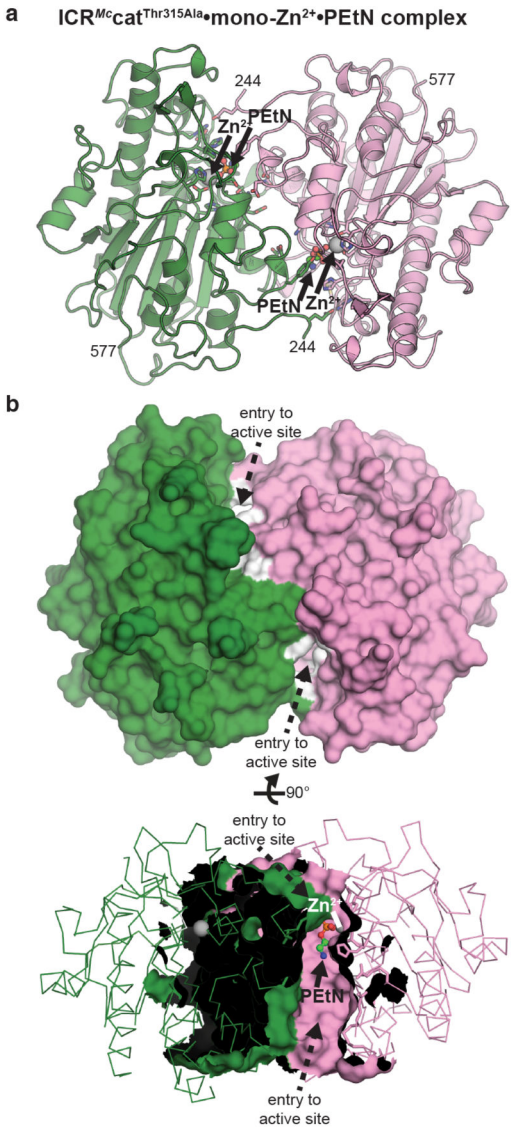

Figure 4.

Structure of dimeric ICR^{Mc}cat^{Thr31SAla}.mono-Zn^{2+}.PEtN complex. (A) Two chains are independently colored. Zn^{2+} shown in gray spheres, PEtN shown in green ball-and-stick. (B) Surface representation. Two entry paths to active sites are labeled. White shading indicates residues in active site clefts. Bottom view is rotated 90° from the top view in the plane of the page and cut-away for visualization into the solvent-occluded active sites.

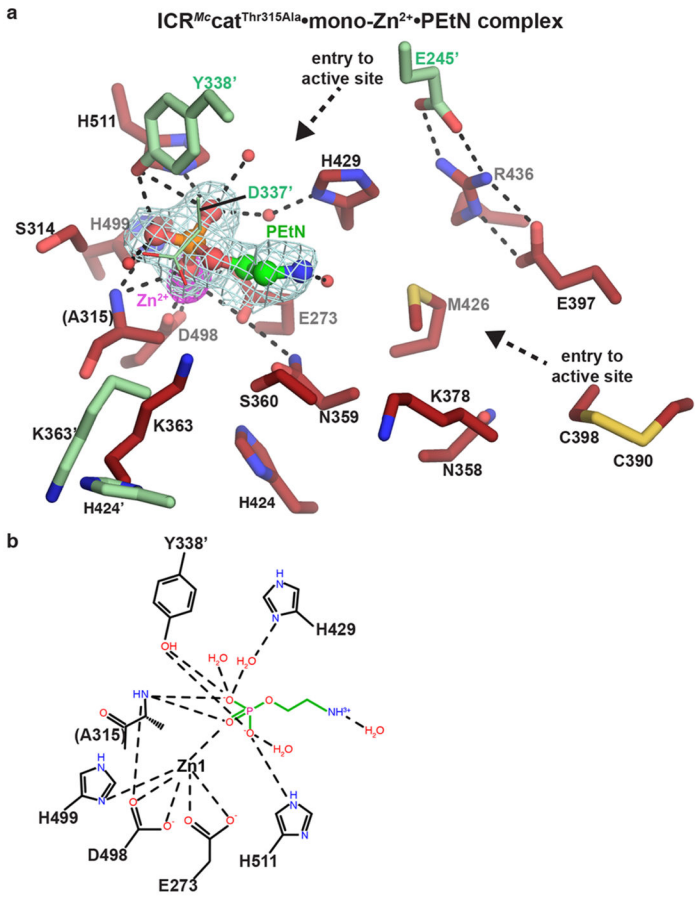

Figure 5.

Active site of dimeric ICR^{Mc}cat^{Thr315Ala}.mono-Zn^{2+}.PEtN complex. (A) Same view is shown as in Figure 3. Residues colored light green are from the partner chain in the dimer. The Zn^{2+} ion is shown as a gray sphere with anomalous difference density contoured at 20σ. PEtN is shown in ball-and-stick with $F_o - F_c$ difference density contoured at 3.0σ. Dashes indicate hydrogen bonds or salt bridge interactions. Water molecules are shown as red spheres. (B) Schematic of Zn^{2+} (shown as Zn1) and PEtN recognition by ICR^{Mc}cat^{Thr315Ala}.

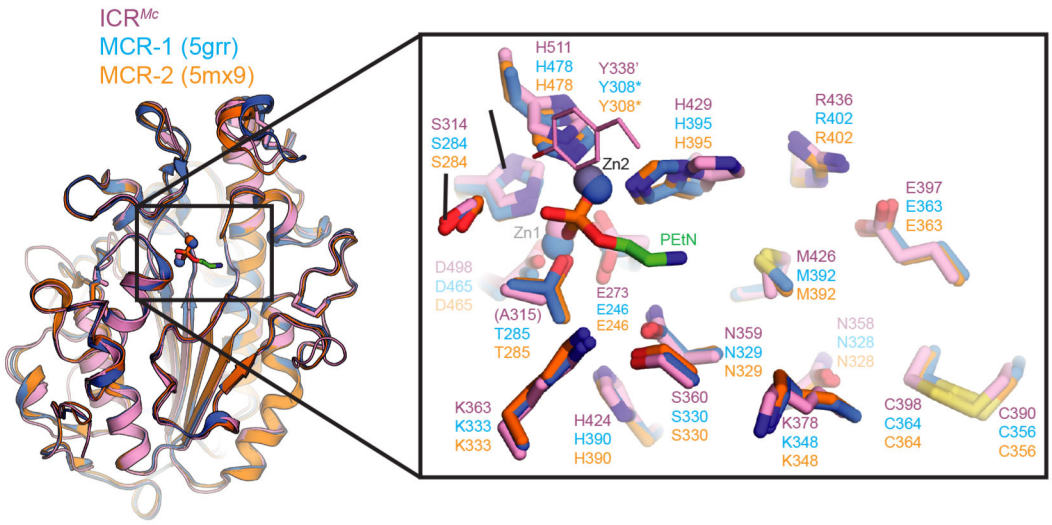

Figure 6.

Comparison of structures of ICR^{Mc}, MCR-1, and MCR-2 catalytic domains. (left) Overall superposition of the three structures, ICR^{Mc} shown in pink, MCR-1 in light blue, MCR-2 in orange. Enlargement shows the active site residues. Parentheses indicate mutation A315 in ICR^{Mc}, asterisks indicate Y308 from MCR-1 and MCR-2 are not shown as their crystal structures were not dimeric. PEtN as bound to ICR^{Mc}cat^{Thr315Ala} is shown in green sticks.

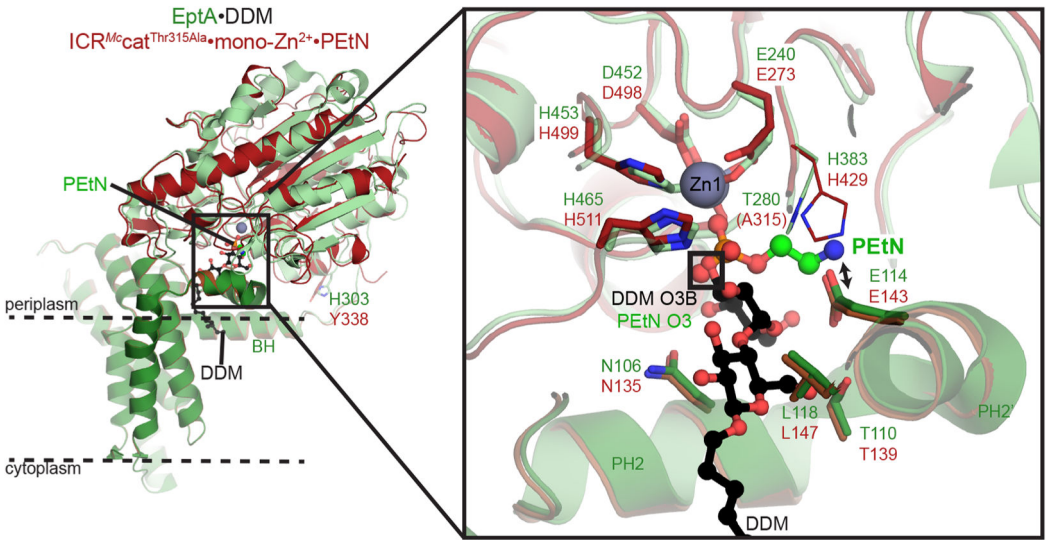

Figure 7.

Model of full-length ICR^{Mc}.mono-Zn^{2+}.PEtN complex based on the structure of *N. meningitidis* EptA. (left) Overall structures, with ICR^{Mc} shown in dark red and EptA in shades of green. DDM as bound to EptA and PEtN as bound to ICR^{Mc} are shown in black and green ball-and-stick, respectively. (dashed lines) Putative plane of inner membrane. (right) Enlargement of active site. Residues interacting with Zn^{2+}, DDM, or PEtN are shown in sticks and labeled. Double-ended arrow indicates close approach of E114/E143 with amine group of PEtN. Box indicates overlap in spatial position of DDM O3B and PEtN O3 atoms. BH = base helix; PH2 and PH2′ = periplasmic helices 2 and 2′ (nomenclature from ref 35).

Table 1.

Heterologous Polymyxin Resistance Conferred by *icr*^{Mc} and *mcr-1*[a]

gene	construct[b]	antibiotic	MIC(μg/mL)
none	none	colistin	0.25
	none	polymyxin B	0.25
icr^{Mc}	pGDP1::*icr*^{Mc}	colistin	2
	pGDP2::*icr*^{Mc}		1
	pGDP1::*icr*^{Mc}Thr315Ala		0.25
	pGDP1::*icr*^{Mc}Tyr338Arg		0.25
	pGDP1::*icr*^{Mc}His429Ala		0.25
	pGDP1::*icr*^{Mc}Arg436Ala		0.25
	pGDP1::*icr*^{Mc}cat		0.25
	pGDP2::*icr*^{Mc}cat		0.25
	pGDP1::*icr*^{Mc}	polymyxin B	2
	pGDP2::*icr*^{Mc}		1
	pGDP1::*icr*^{Mc}Thr315Ala		0.25
	pGDP1::*icr*^{Mc}Tyr338Arg		0.25
	pGDP1::*icr*^{Mc}His429Ala		0.25
	pGDP1::*icr*^{Mc}Arg436Ala		0.25
	pGDP1::*icr*^{Mc}cat		0.25
	pGDP2::*icr*^{Mc}cat		0.25
mcr-1	pGDP1::*mcr-1*	colistin	4
	pGDP2::*mcr-1*		4
	pGDP1::*mcr-1*cat		*c*
	pGDP2::*mcr-1*cat		0.25
	pGDP1::*mcr-1*	polymyxin B	4
	pGDP2::*mcr-1*		4
	pGDP1::*mcr-1*cat		*c*
	pGDP2::*mcr-1*cat		0.5

[a] Susceptibility testing was performed with *E. coli* BW25113.

[b] pGDP1 = P_{bla} promoter; pGDP2 = P_{lac} promoter.

[c] No data.

Table 2.

X-ray Diffraction Data Collection and Refinement Statistics

structure	**ICR^{Mc}.PO$_4$ complex**	**ICR^{Mc}.mono-Zn^{2+} complex**	**ICR^{Mc} T315A.di-Zn^{2+}.PEG complex**	**ICR^{Mc} T315A.mono-Zn^{2+}.PEtN complex**
PDB code	6BNE	6BNF	6BNC	6BND
		Data Collection		
space group	$P4_132$	$P4_132$	$P2_12_12$	$P2_12_12$
cell dimensions, *a*, *b*, *c* (Å)	147.52	148.27	74.05, 154.25, 66.39	74.52, 155.24, 66.41
resolution, Å	104.32–2.61	104.84–2.33	30.00–1.50	31.80–1.64
R_{merge} [a,b]	0.181 (3.313)	0.161 (3.941)	0.088 (0.595)	0.108 (1.950)
R_{pim} [b]	0.028 (0.515)	0.025 (0.672)	0.026 (0.203)	0.044 (0.827)
$CC_{1/2}$ [b]	0.840	0.841	0.982	0.594
$I/\sigma(I)$ [b]	24.7 (2.6)	24.0 (2.0)	30.68 (4.1)	14.5 (1.3)
completeness, [b] %	100 (100)	100 (100)	99.9 (100)	100 (100)
redundancy [b]	77.3 (79.5)	76.5 (66.5)	11.9 (8.8)	13.4 (12.6)
		Refinement		
resolution, Å	60.23–2.61	46.88–2.33	29.82–1.50	31.81–1.64
no. unique reflns: working, test	16528, 830	23489, 2163	121223, 10848	94685, 3840
R-factor/free *R*-factor [b,c]	23.6/27.1 (48.0/48.7)	20.9/24.8 (40.8/46.4)	13.2/15.3 (19.8/23.4)	15.1/19.2 (34.2/32.7)
no. of refined atoms, molecules				
protein	2602	2607	5293	5255
zinc	N/A	1	4	2
phosphate [d]	5	5	N/A	N/A
sulfate [d]	5	5	N/A	N/A
PEtN	N/A	N/A	N/A	16
other solvent	20	42	103	37
water	116	209	1093	1128
B-factors				
protein	79.1	67.8	17.3	26.9

structure	ICR^{Mc}.PO$_4$ complex	ICR^{Mc}.mono-Zn^{2+} complex	ICR^{Mc} T315A.di-Zn^{2+}.PEG complex	ICR^{Mc} T315A.mono-Zn^{2+}.PEtN complex
zinc	N/A	63.8	11.2	26.9
phosphate[d]	108.0	82.0	N/A	N/A
sulfate[d]	87.6	78.6	N/A	N/A
PEtN	N/A	N/A	N/A	29.1
other solvent	116.2	95.0	29.3	22.9
water	65.44	66.6	36.2	46.2
rmsd				
bond lengths, Å	0.006	0.006	0.002	0.017
bond angles, deg	1.380	1.274	1.468	1.319

[a] $R_{\text{merge}} = \Sigma_h \Sigma_i \mid I_i(h) - \langle I(h) \rangle \mid / \Sigma_h \Sigma_i I_i(h)$ where $I_i(h)$ and $\langle I(h) \rangle$ are the ith and mean measurement of the intensity of reflection h.

[b] Figures in parentheses indicate the values for the highest resolution shells of the data.

[c] R-factor $R\text{-factor} = \Sigma \mid F_p^{obs} - F_p^{calc} \mid / \Sigma F_p^{obs}$ where F_p^{obs} and F_p^{calc} are the observed and calculated structure factor amplitudes, respectively.

[d] Molecules in the active site cleft.

ACS Chem Biol. Author manuscript; available in PMC 2018 October 22.